Supplementary Materials for:

Carbon dioxide sources from Alaska driven by increasing early winter respiration from Arctic tundra by R. Commane, J. Lindaas, J. Benmergui, K. A. Luus, R. Y.-W. Chang, B. C. Daube, E. S. Euskirchen, J. M. Henderson, A. Karion, J. B. Miller, S. M. Miller, N. C. Parazoo, J. T. Randerson, C. Sweeney, P. Tans, K. Thoning, S. Veraverbeke, C. E. Miller, S. C. Wofsy

SM1. Aircraft Observation Framework

The flight sampling strategy was optimized for the column-analysis employed in this work, and is described in Sections SM1-3.

SM1.1 Aircraft Measurements

Carbon in Arctic Reservoirs Vulnerability Experiment (CARVE) flights were conducted over Alaska between 2012 and 2014. The NASA C-23B (N430NA) aircraft, based in Fairbanks, Alaska, USA flew over most of Alaska, excepting the south-east panhandle, covering areas from 55° to 72°N and 165° to 140°W. Flights were made during approximately two weeks of each month between May and September 2012, April and October 2013, and May and November 2014. Each sub-region of the state was usually sampled once during each measurement period so the CARVE data can assess the regional fluxes, but, as for most flight programs, the aircraft could not fully characterize the diurnal or daily variations of CO_2 concentrations or fluxes. As the CARVE project progressed, the importance of the early winter cold season respiration became more evident, motivating flights through mid-November 2014, despite the challenge of operating a C-23B so late in the season.

Mole fractions of CO_2, CH_4 and CO were measured using two independent cavity ringdown spectrometers: one operated without drying the sample air (G1301-m in 2012 **(*1*)** and G2401-m from 2013) and one dried (G2401-m **(*2*)**). Each analyzer was calibrated throughout the flights, mutually gap filling to ensure a continuous 5 s time series. Mole fractions of CO_2 are presented as μmol per mol of dry air, or parts per million (ppm). The aircraft measurements were aggregated horizontally every 5 km and vertically in 50 m intervals below 1 km (above sea level; asl) and 100 m intervals above 1 km **(*2*)**.

We identified 273 profiles of ≤ 30 minutes duration where the transition between the atmospheric residual layer (maximum height influenced by surface emissions during transit from the boundary layer; cf. ***3***) and the free troposphere was evident (usually at altitudes ≥ 3 km). Figure S1 shows altitude profiles of observed and modeled (SM2) CO_2 mole fractions for (A) 7th June and (B) 9th November 2014, and (C) flight tracks of data used in the analysis below. For each altitude profile measured by the aircraft, we calculate the column enhancement of CO_2 above the regional background (SM1.3) for altitudes below the top of the residual layer (SM1.2).

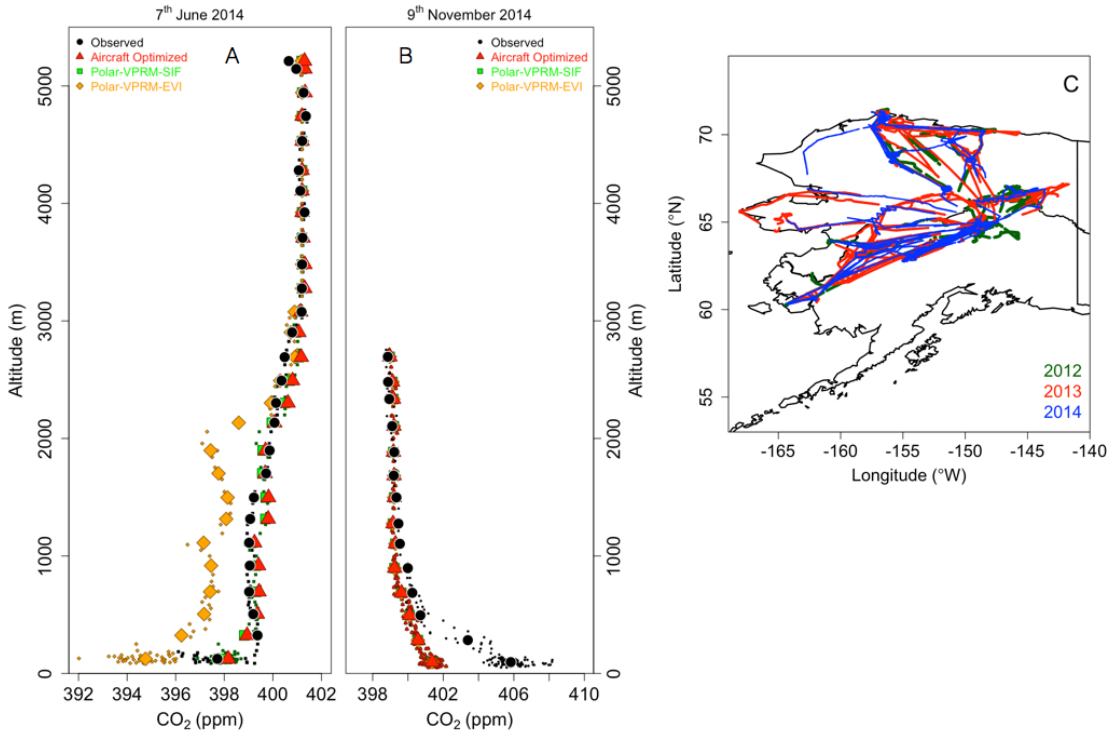

Fig S1: ***An altitude profile*** *in (A) June 7th 2014 and (B) November 9th 2014 that show the atmospheric structure typical of CARVE flights for individual measurements (small points) and 200m binned averaged (large points) for observations (black), CO_2 enhancements (above the background identified for the column) calculated using PVPRM-SIF (green), PVPRM-EVI (orange) and the aircraft optimized flux (red). B illustrates that calculating the mean additive flux for the flight period may result in an underestimation of the flux on some individual days. Note: all model points are hidden behind the aircraft optimized data (in red) (C) shows the spatial distribution of the data used in the column enhancement analysis (SM2).*

SM1.2 Column Enhancement of CO_2

The column enhancement of CO_2 mole fractions represents the mass loading of regional emissions in the atmosphere from the surface to the top of the atmospheric residual layer. The column enhancements for each profile were calculated by block averaging the observed CO_2 dry mole fraction ($[CO_2]$) into 200 m altitude bins and subtracting the background CO_2 and then integrating the density-weighted mole fraction enhancement:

$$CE_{CO_2} = \int_0^h ([CO_2](z) - [CO_2]_{(0)}) \frac{P(z)}{RT(z)} dz \quad (1)$$

where $[CO2]_0$ is the background CO_2 mole fraction (SM1.3), P and T are the pressure and temperature of dry air within the bin respectively and R is the universal gas constant.

Atmospheric column enhancements have been used in CO_2 studies in the Amazon **(e.g. *3-5*)** and in CH_4 flux determinations from CARVE data in Alaska **(*2*)**). The mean CO_2 mole fraction at altitudes above the residual layer provides an estimate of the background value for each profile (SM1.3). The value of the background concentration and height of the residual layer were identified from the vertical structure of the CO_2, CH_4, CO, O_3, water vapor and temperature profiles. The column enhancement of CO_2 depends mainly on the large-scale simulation of the vertical structure of the atmosphere, reducing the influence of fine details of the convective boundary layer and residual layer, fine-scale variations of emissions at the surface, and turbulent transport in the lower atmosphere.

Our Lagrangian transport model (WRF-STILT, SM2.1) reproduces the structure of atmospheric CO_2 for most of the profiles we obtained in Alaska. Some aspects of the data set cannot be reproduced by the transport model:

1. The aircraft long runs at altitudes below ~1 km, frequently following the orography of the domain, e.g. sampling in river valleys. However, such orographic features - with horizontal spatial scales less than ~3 km cannot be resolved by the atmospheric transport model.
2. WRF-STILT does not resolve individual eddies in the boundary layer. Associated errors are minimized by considering the column enhancements which average over the entire residual-layer, with a characteristic length of 10s to 100s of km.
3. Profiles were acquired throughout the day, including during early morning when the previous night's very thin boundary layer was still present. This condition was not well simulated by WRF. The diurnal range in the CO_2 flux is particularly large in summer, amplifying the effect of any incorrect calculation of the nocturnal boundary layer height or the timing of the growth of the early morning boundary layer.

Our selection of vertical profiles incorporates 85% of all CARVE profiles of height 3 km or higher (231 of 273). The remainder were excluded because of biomass burning influence (CO > 150 ppb), unresolved or chaotic atmospheric structure, or >30% influence from non-Alaskan land areas (usually from Siberia).

SM1.3 Background CO_2 Comparison

Background CO_2 values represent the CO_2 mole fraction in air entering the Alaskan airshed (i. e. before changes due to CO_2 uptake or emission from the Alaskan land surface) and, for the aircraft analysis, they were calculated from the mean CO_2 mole fraction above the residual layer (Fig. S2, red diamonds). We compared the seasonal cycle of these free troposphere backgrounds to the Alaskan CO_2 background estimated from the CRV and BRW long-term measurement towers within Alaska. For the CRV tower **(SM4.1, *6*)**, the transport of 500 particles for each atmospheric mole fraction observation were traced back to either where they left the domain or to their location after 10 days, if they

were still inside the domain, using the WRF-STILT Lagrangian transport model (**SM2.1**). Using these positions and times, background CO_2 values were taken to be the corresponding CO_2 mole fraction from an empirically derived boundary curtain calculated by fitting observations from NOAA/ESRL long-term sites **(6, *7*)** (Fig S2, black circles). For the BRW tower (described in **SM4.2**), the CO_2 background values are the CO_2 mole fraction in air from the ocean or "clean air" sector (Fig. S2, blue squares). Figure S2 shows that the background CO_2 values for each of the methods generally compare well across the seasonal cycles.

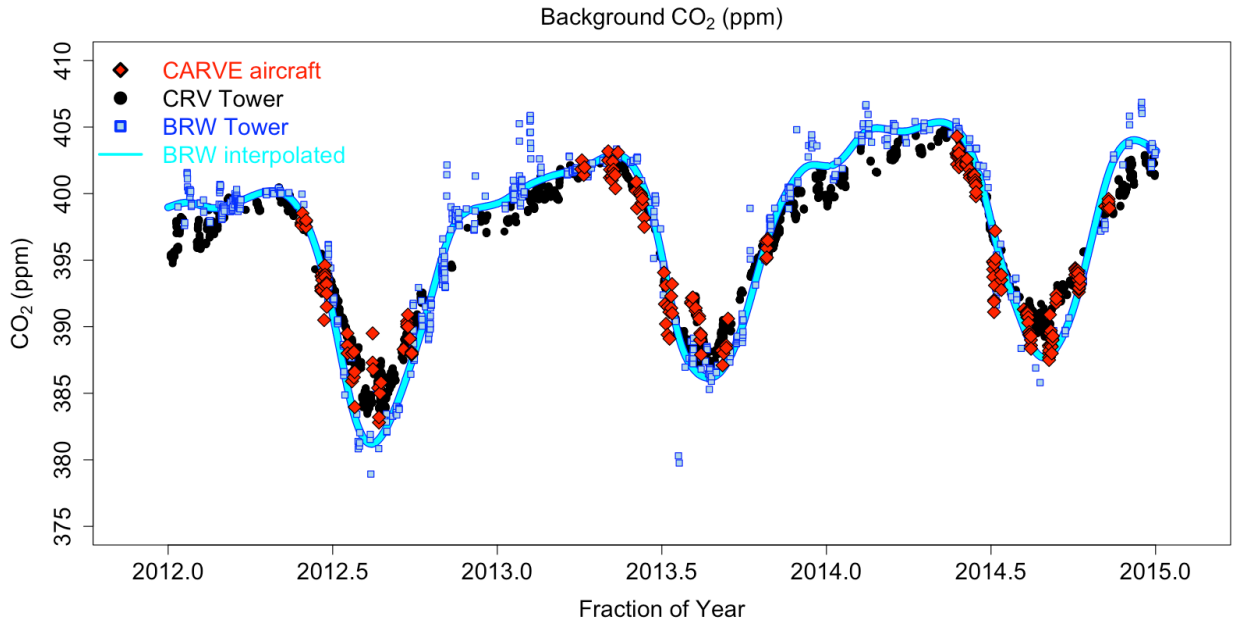

Fig S2: ***Background CO_2 mole fractions.*** *Background of CO_2 of the CARVE aircraft profiles (red diamonds), the CRV tower (black circles) and the BRW tower clean ocean data and interpolated background (blue squares and cyan line). The latitudinal gradient in the background CO_2 is especially evident in summer between the CRV tower (~65.0°N) and the BRW tower (~71.3°N).*

SM2. Framework to predict integrated CO_2 column

For each aircraft integrated CO_2 column (SM1.2), we coupled a high resolution transport model (SM2.1) with a data-driven CO_2 flux estimate (SM2.2) to predict atmospheric CO_2 enhancements associated with Alaskan land surface biogenic fluxes, and then we calculated the modeled integrated CO_2 column.

SM2.1. Transport Model

A polar variant of version 3.5.1 of the Weather Research and Forecasting (WRF v3.5.1) model, with 3.3 km grid spacing in the innermost domain over Alaska, was used to drive the Stochastic Time-Inverted Lagrangian Transport model **(STILT; *8*)** . Each binned data

point (SM1.1) was treated as a receptor for the STILT model. STILT follows the trajectory of 500 air parcels (particles) released from the receptor position backwards in time over the previous 10 days, where the motion of each parcel includes advection by the large-scale wind fields and random turbulent motion, independent of the other parcels. The proportion of particles residing in the lower half of the planetary boundary layer determined the influence of surface fluxes on the measured mole fractions. The two dimensional "footprint" is calculated for each particle at 3 hour intervals on a 0.5° by 0.5° grid over the 10-day travel period of the particles, defined as the response of each receptor measurement to a unit emission of CO_2 at each grid square (units: µmol mol^{-1}/ µmol m^{-2} s^{-1}). The WRF-STILT simulations used here were specifically generated for CARVE data analysis, with both the WRF meteorology simulations and the STILT particle trajectories evaluated in detail **(2)**. Figure S3 displays the monthly cumulative land surface influence observed from the aircraft data over the domain for each month during 2012-2014, indicating the overall sampling density of CARVE flight data used in this study.

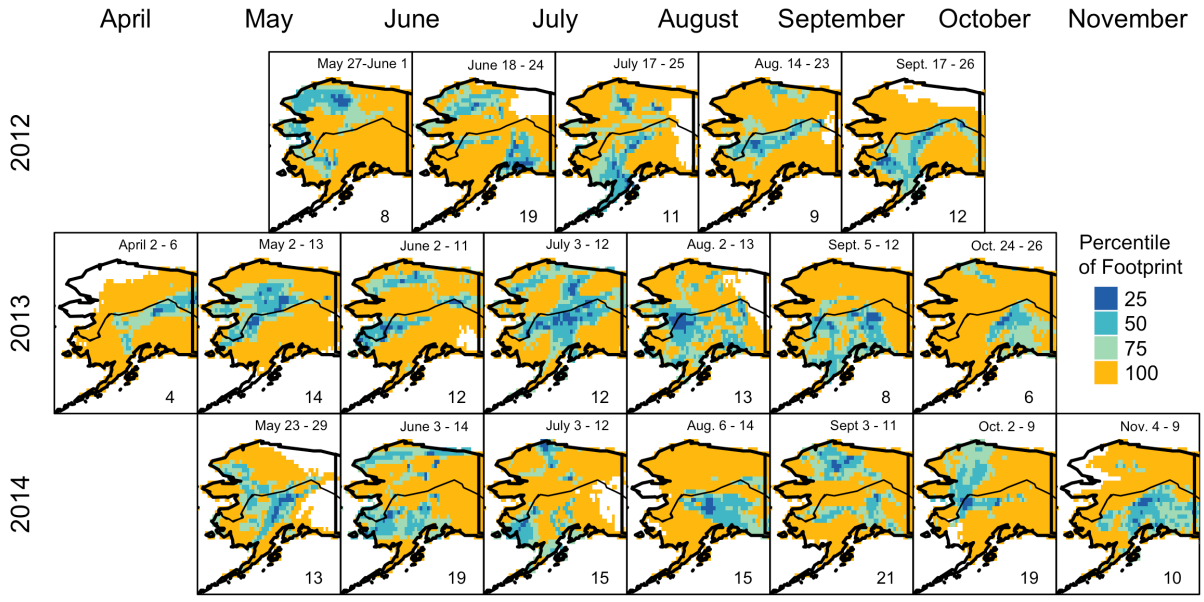

Fig S3: ***Monthly composite of the percentile of surface influence of profiles*** *used in our analysis within a given month for April - November 2012-2014. The date range of the profiles is shown at the top and the number of profiles in each month at the bottom right of each map. The top row is offset as the flights were made during the last two week of each month in 2012 and during the first two weeks of each month in 2013 and 2014. White areas indicate no land surface influence within the profiles for that month.*

SM2.2. Calculating biogenic CO_2 fluxes

Spatially explicit, time varying ecosystem fluxes of CO_2 were calculated using the Polar Vegetation Photosynthesis and Respiration Model **(PVPRM, *9*)**. These were used in our inverse analysis as a deterministic predictor of atmosphere-biosphere exchange rates of CO_2. The PVPRM is a functional representation of ecosystem CO_2 fluxes from which we generate high resolution (three hourly, 1/6° x 1/4° latitude/longitude grid) data-driven estimates of net CO_2 ecosystem exchange (NEE). The variations of NEE for three-hourly, diurnal and seasonal intervals are captured by using assimilated meteorological inputs from North American Regional Reanalysis **(NARR, *10*)**, and solar induced chlorophyll fluorescence (SIF) from Global Ozone Monitoring Experiment 2 **(GOME-2, *11*)**. Previous versions of PVPRM also used land surface inputs from Moderate Resolution Imaging Spectroradiometer **(MODIS, *12–15*)**.

PVPRM calculates NEE as the sum of autotrophic and heterotrophic respiration (R_{eco}), and gross ecosystem productivity (GEP). R_{eco} is calculated as a linear step-wise function of NARR soil and air temperatures for snow (winter) and growing (summer) seasons, respectively. Snow/growing seasons are distinguished using snow cover area (SCA) data from MODIS **(*14*)** (and shown as Eqn 6 from **(*16*)**).

$$R = \begin{cases} \alpha_a \cdot T_a + \beta_a, & \text{if } SCA < 50\% \\ \alpha_s \cdot T_s + \beta_s, & \text{if } SCA \geq 50\% \end{cases} \quad (2)$$

GEP is simulated as a function of air temperature (2m T_{air} from NARR), photosynthetically active radiation (PAR, scaled to NARR SW radiation), and fraction of PAR absorbed by photosynthetically active radiation (f_APAR). We estimate f_APAR SIF from GOME-2 satellite (*11*, as used in the main analysis of this paper):

$$\text{GEP} = \lambda \cdot T_{scale} \cdot \frac{SIF}{cos(SZA)} \cdot \frac{1}{1 + \frac{PAR}{PAR_0}} \cdot PAR \quad (3)$$

$$T_{scale} = \frac{(T_{air} - T_{min})(T_{air} - T_{max})}{(T_{air} - T_{min})(T_{air} - T_{max}) - (T_{air} - T_{opt})^2} \quad (4)$$

where T_{max} = 40°C, T_{min} = 0°C for all vegetation classes and T_{opt} =15°C for tundra vegetation and T_{opt} = 20°C for boreal vegetation and PAR_0 are coefficients determined for each ecosystem class **(*9*, *17*)**. There are also SIF data from the OCO-2 (Orbiting Carbon Observatory 2) satellite **(*18*)** from September 2014 onwards that can be used in place of GOME-2 in future work.

Coefficients for PVPRM-SIF were obtained for each vegetation class using eddy covariance measurements of CO_2 fluxes, site-level meteorology and remote-sensing data (as described for EVI in **(*17*)** and for PVPRM-SIF in ***(9)***. Flux fields for PVPRM-SIF are

available in **(*19*)**. We used seven vegetation classes identified from the circumpolar Arctic vegetation map (CAVM) **(*20*)** above the northern tree line and the Synergistic Land Cover Product (SYNMAP) south of the tree line **(*21*)**. The combined CAVM-SYNMAP vegetation classification is available 1/120° x 1/120° resolution. Figure S4 shows the monthly mean NEE predicted for the domain during the CARVE observation period (2012-2014), before the optimization (**SM3**).

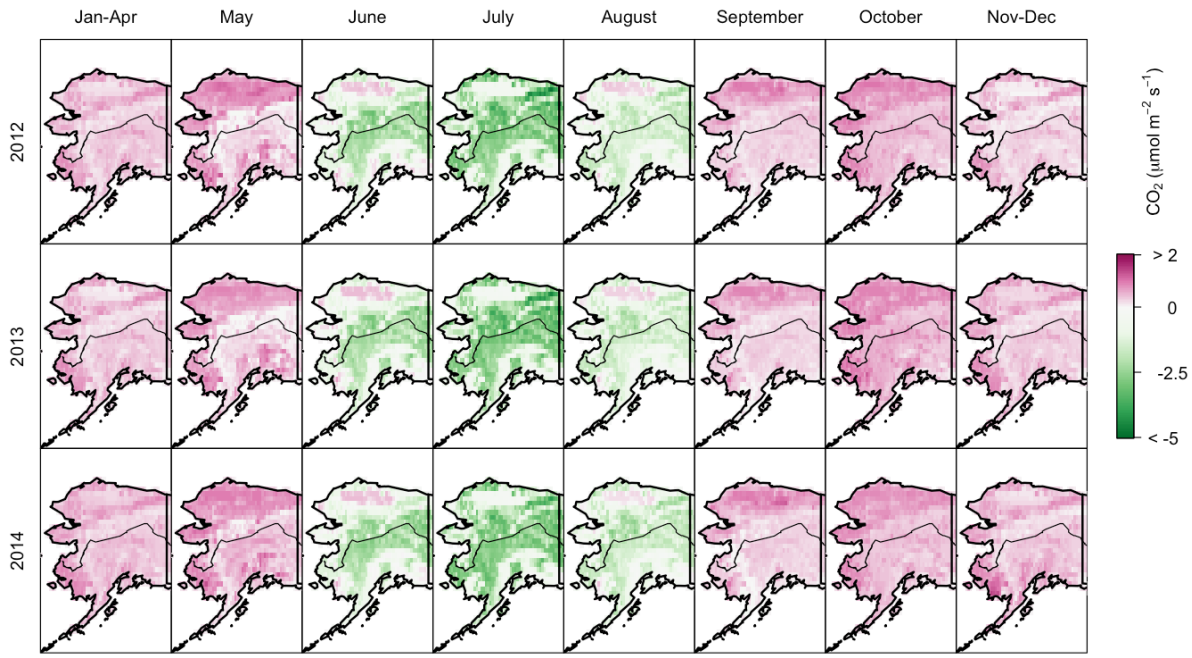

Fig S4: *Monthly mean predicted biogenic net flux of CO_2 (NEE) for the Alaskan domain for 2012-2014 from PVPRM-SIF (**SM2.2**). Fluxes during January-April showed minimal variability and were combined for clarity, as were fluxes from November and December. PVPRM-SIF predicts large uptake in the summer months of June-August and respiration throughout the rest of the year. These predicted fluxes are the basis of the optimization using the aircraft data.*

The original formulation of the VPRM used the Enhanced Vegetation Index (EVI, denoted PVPRM-EVI), along with empirical "phenology" factors, as the measure of plant light use efficiency **(*17*)**. It was further developed for polar regions in Luus et al., (2017) **(*9*).**

$$GEP = \lambda \cdot EVI \cdot T_{scale} \cdot P_{scale} \cdot \frac{1}{1 + \frac{PAR}{PAR_0}} \cdot PAR \qquad (5)$$

where P_{scale} is a function of the MODIS Land Surface Water Index (LSWI, ***15***).

Figure S4 shows the monthly mean CO_2 flux for Alaska throughout 2012-2014. Note that the transitional months of June and August indicate net neutral fluxes in some locations (e.g. snow melt and subsequent photosynthesis occurs in mid-June on the North Slope of Alaska). The timing of the calculated net uptake coincides with that of year-round eddy flux data from tundra (***22-24***) and boreal forest (***25, 26***) ecosystems. Figure S5 shows the time series of PVPRM-SIF, PVPRM-EVI and the optimized flux. Initially the optimization (**SM3**) used predicted CO_2 fluxes calculated by PVPRM-EVI (which has EVI and P_{scale} representing seasonal productivity) but a strong early spring bias was evident in all years (2012 is highlighted in Fig. S5). In an effort to understand the cause of this spring bias, we modified PVPRM to include SIF as the driver of seasonal phenology instead of EVI and P_{scale}. Fluxes calculated using PVPRM-SIF did not show the early spring bias evident in the PVPRM-EVI when compared to the optimized fluxes. Therefore, we used the CO_2 fluxes calculated using PVPRM-SIF in our detailed analysis below.

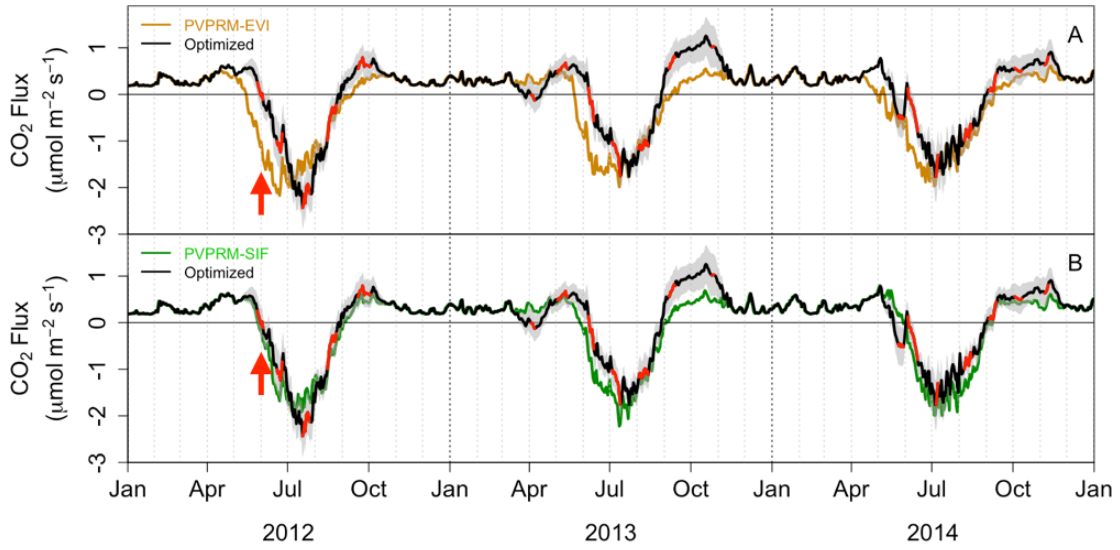

Fig S5: ***Mean Alaskan biogenic CO_2 flux for 2012-2014.*** *Mean daily CO_2 flux for Alaska calculated from* ***A:*** *PVPRM-EVI (orange) and* ***B*** *PVPRM-SIF (green). The data constrained optimized flux (black and red, SM2.5). Time periods constrained by aircraft observations are shown in red. Gray shading indicates the uncertainty in the optimized fluxes. Red arrows highlight the timing of the spring bias in 2012 but the bias was also evident in 2013 and 2014.*

3. Calculation of the Additive Flux Correction

We calculated the additive flux correction required to match the modeled to observed column enhancements, within a given measurement period using the methods described in this section. The "column difference" calculated for each flight period was defined as the difference between the modeled and observed integrated CO_2 columns. To represent the spatial distribution of the additive flux correction we applied an inverse model to the column difference for each two week flight period. The column differences vary between -0.25 to +0.45 mol m^{-2}. The goal of the inverse framework is to find an optimal model of the additive flux correction that accounts for the spatial variations of the column differences for each flight period, leading to a spatially explicit, optimal estimate for the CO_2 fluxes and annual budget for Alaska.

3.1. Inversion Methodology

We used a geostatistical approach ***(27)*** that optimizes the additive flux correction (**s**) given the column differences (**z**), the WRF-STILT surface influence (a.k.a., the Jacobian) (**H**), and two error covariance matrices (with error (ϵ):

$$\mathbf{z} = \mathbf{Hs} + \epsilon \tag{6}$$

with *n* column differences and *m* elements of the additive flux correction, the Jacobian (**H**) has dimension *n x m*. Each row of the Jacobian (**H**) is the WRF-STILT surface influence for a given column difference. We do not use a prior flux estimate in the same way as in a more conventional Bayesian inverse model. In place of a conventional prior, (an independent direct estimate of the fluxes), we use a linear combination of auxiliary variables (the “deterministic component” of the model). We add a Gaussian random field (the “stochastic component” of the model), which adjusts the additive correction to optimally fit the model to the observations, within the error. Such a model has utility when reliance on a conventional prior would have detrimental effects (e.g., the conventional prior would be biased against the observations).

The model calculates the optimal additive flux correction ($\hat{\mathbf{s}}$) and drift coefficients ($\boldsymbol{\beta}$) that maximize the posterior probability distribution function ($p(\mathbf{s}, \boldsymbol{\beta} | \mathbf{z}, \mathbf{H}, \mathbf{R}, \mathbf{X}, \mathbf{Q})$):

$$\mathrm{p}(\mathrm{s}, \beta \mid \mathrm{z}, \mathrm{H}, \mathrm{R}, \mathrm{X}, \mathrm{Q}) \propto exp[\frac{-1}{2}(\mathrm{z}-\mathrm{Hs})^{\mathrm{T}}\ \mathrm{R}^{-1}\ (\mathrm{z}-\mathrm{Hs}) - \frac{-1}{2}(\mathrm{s}-\mathrm{X}\beta)^{\mathrm{T}}\ \mathrm{Q}^{-1}\ (\mathrm{s}-\mathrm{X}\beta)], \tag{7}$$

where:

z is an *n x 1* vector of column differences (units mol m^{-2})

s is an *m x 1* vector of additive fluxes (units µmol m^{-2} s^{-1})

H is an n *x m* Jacobian matrix of column integrated surface influence (units (mol m^{-2})/ (µmol m^{-2} s^{-1}))

X is an *m x p* matrix of *p* auxiliary variables (units vary in accordance with each variable)
β is a *p x 1* vector of drift coefficients (units such that the units of **X**β are µmol m^{-2} s^{-1})
R is an *n x n* 'model-data mismatch error' covariance matrix (units $(\text{mol } m^{-2})^2$)
Q is an *m x m* 'prior error' covariance matrix (units $(\mu\text{mol } m^{-2} s^{-1})^2$).

As described in **(*28*)** (Equations 25-30), the posterior probability distribution function (Eqn. 7) can be maximized analytically to yield the optimal estimate of the additive flux correction. The error covariance matrix of the optimal estimate of the additive flux correction can also be calculated analytically.

3.2. Additive Flux Correction Result

Figure S6 shows the residual column differences after the additive flux correction has been applied for the years (A) 2012, (B) 2013, and (C) 2014. Figure S6 (D) shows a plot of the residuals column differences against the fitted values. To evaluate the distribution of these residuals, we normalize the residuals from each month with respect to their standard deviation (studentize) and plot them against the theoretical normal distribution (Fig. S6 (E)). The values on the normal Q-Q plot all lie close to the 1-1 line, demonstrating that they are well described by a normal distribution. The purpose of studentizing the residuals is to be able to plot them with a common axis.

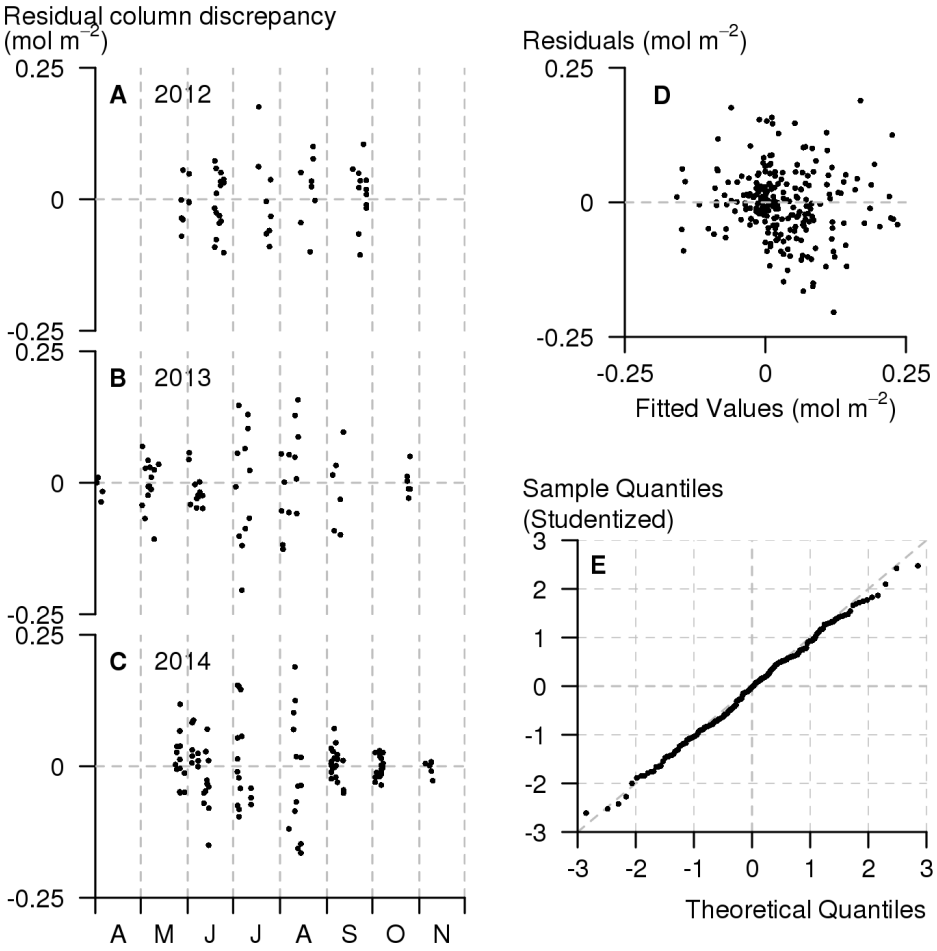

Fig S6: *Residual column differences from the additive flux optimization for the years (A) 2012, (B) 2013, and (C) 2014. (D) A plot of residuals vs fitted values shows no trend in the residuals. (E) A Q-Q plot of residuals normalized each month by their standard deviation (studentized) shows that the distribution of residuals is well described by a normal distribution.*

Figure S7 shows the maximum likelihood *a posteriori* estimate of the additive flux for each flight period. This realization of the additive flux is based on the spatial distribution estimated from PVPRM- SIF respiration, which is based on eddy flux data extend to the region using our map of ecosystem types and meteorological drivers. The optimized CO_2 fluxes (Fig. S8) are the sums of the additive flux and the PVPRM-SIF CO_2 fluxes.

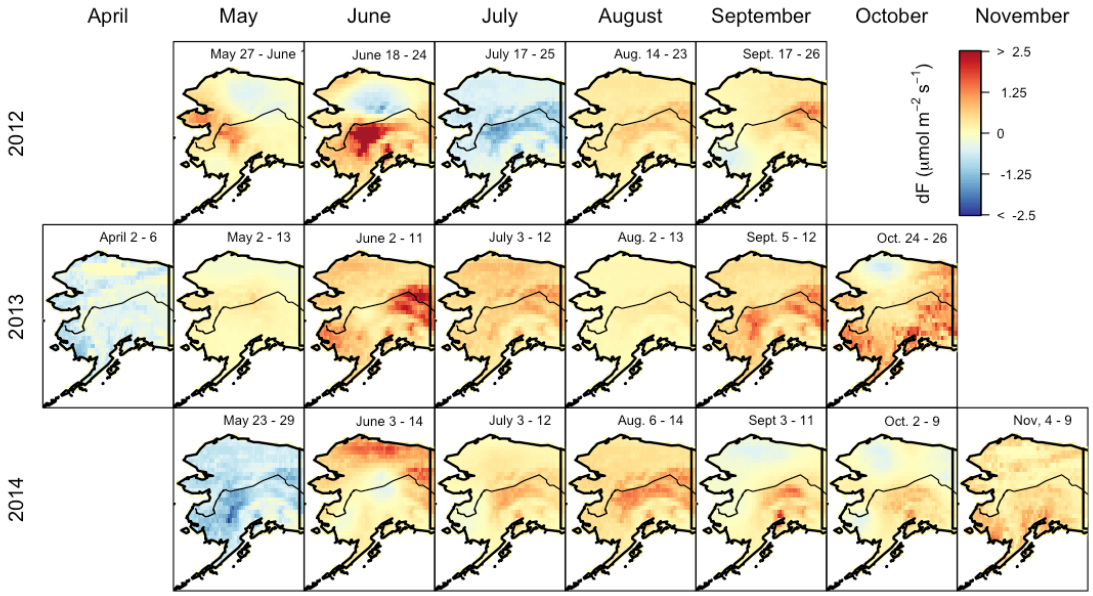

Fig S7: *Spatially resolved additive flux calculated from CARVE aircraft column differences. This realization uses the spatial distribution of respiration as a basis of the optimization.*

The choices of auxiliary variables to be included in **X** are important for the inverse analysis. The auxiliary variables provide a means to regularize the under-constrained inverse modeling problem. It is important to choose a set of auxiliary variables with the greatest predictive power possible, while minimizing the number of adjustable variables to avoid overfitting the data. We initially selected candidate auxiliary variables including PVPRM-SIF predicted respiration (based on soil temperature during snow cover and air temperature during the summer) and/or photosynthesis, ecosystem classes (forest, tundra, and tundra separated into north slope and south-western regions), the presence of the zero curtain (soil temperatures close to 0°C as defined in **(*29*)** and predicted by NARR meteorology), and an intercept term, which accounts for the regional mean flux.

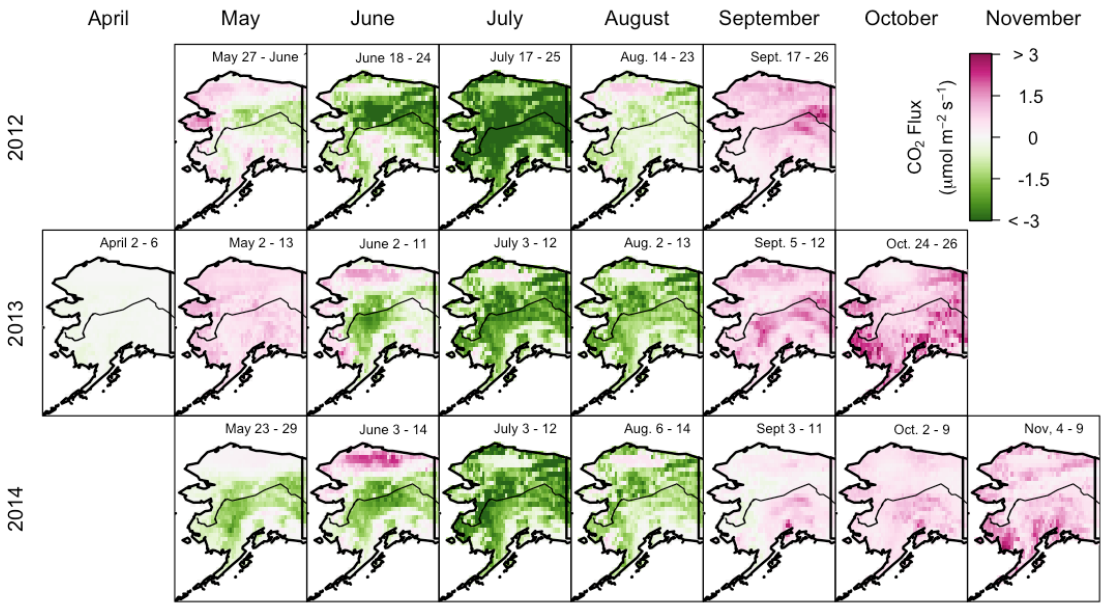

Fig S8: ***Optimized Biogenic Net CO_2 flux for Alaska 2012-2014.*** *The date of each measurement period is shown at the top of each map. We used the additive flux in Fig. S7 adjust the PVPRM-SIF CO_2 flux as seen in Fig S4.*

We determined an optimal set of candidate auxiliary variables using the leave-one-out cross validation (LOOCV) method **(*30-31*)** and the Bayesian Information Criterion (BIC) method **(*32–37*)**. We found that of 80 possible options, the best performing model used either PVPRM-SIF predicted respiration with no intercept term (selected by LOOCV) or just the intercept term (selected first by BIC and selected second by LOOCV). We calculated the budget of each region given by (A) the optimized flux with PVPRM-SIF predicted respiration as an auxiliary variable and (B) the optimized flux with only the intercept term as an auxiliary variable (Fig. S9). The Alaskan net CO_2 budget is insensitive to the choice of auxiliary variable. If we use the regional mean, we estimate slightly more emission from the "Mixed" region emission and more uptake in the boreal forest region, than the respiration variable. Both inversions find the same optimized regional net flux. The changes in the spatial distribution of the flux are small because the PVPRM provides an excellent fit to the observations before the optimization is applied.

3.3. Uncertainty Estimate

The uncertainty of the optimized additive flux is calculated from the error covariance matrices and the Jacobian. **R** is the "model-data mismatch error" covariance matrix, which includes (but is not limited to) errors in modeled atmospheric transport and vertical structure, the spatio-temporal aggregation of fluxes, and errors in the observations, including uncertainty in the observed background mole fractions. **Q** is the "prior error" covariance matrix which controls the variances and covariances of the stochastic component. We constructed parameterized models for **R** and **Q** and fit the parameters using restricted maximum likelihood estimation (ReML) **(*30*)**. We modeled **R** as a diagonal ma-

trix with constant elements, σ_R^2. We modeled **Q** with an exponential decay in space (with a length scale ϕ), and diagonal elements given by a scaled PVPRM-SIF predicted respiration (with a scaling parameter σ_Q^2).

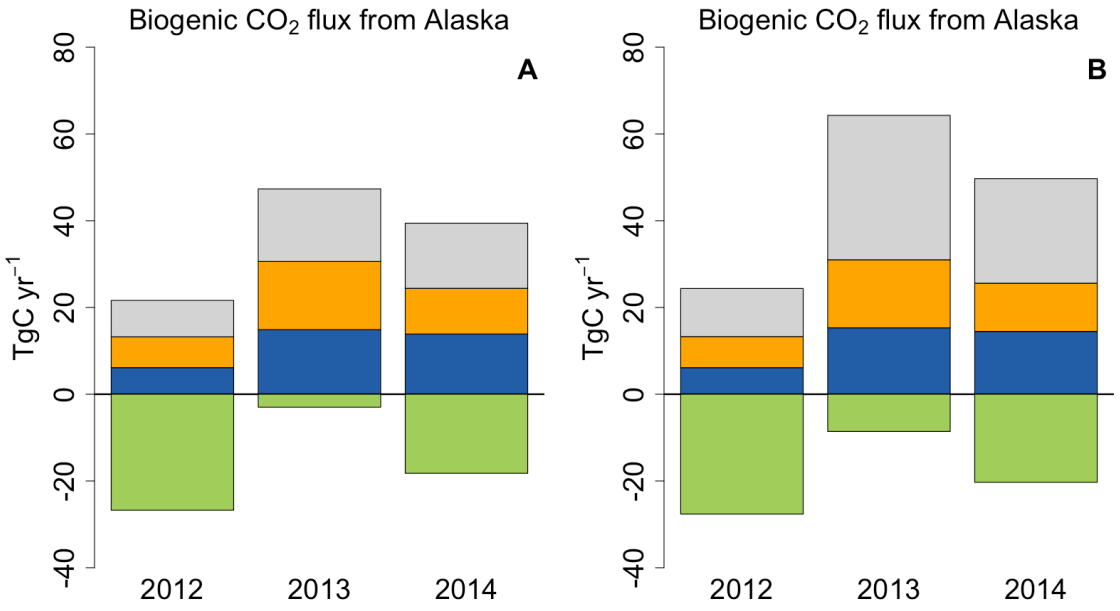

Fig S9: ***Annual biogenic budget with additive correction based on (A)*** *PVPRM-SIF respiration and* ***(B)*** *the "flat" model of no spatial contribution for each region: Mixed (gray), South-west Tundra (orange), North Slope tundra (blue) and Boreal (green). The net budget does not change based on the method used but there are small differences in the regional attribution, with increased uptake in the boreal and emission from the mixed areas in the flat model.*

We derived the optimal additive flux correction for each flight period (~2 weeks each month) independently and assume that prior errors are correlated within a flight period and uncorrelated across flight periods. There are insufficient data in an individual month to constrain the error statistics with ReML. We therefore used ReML to constrain a climatology of error statistics by combining data from all years for each month (and also combining April with May and October with November). Additionally, the de-correlation length scale (ϕ) was poorly constrained by ReML, and so we performed an additional LOOCV test to find the length scale that minimized the RMSE of LOOCV, $\phi \sim 300$ km.

We generated 10,000 realizations of the additive flux correction (dF) and added that to the raw CO_2 flux calculated from PVPRM-SIF (F_{CO2}) (see ***(61)*** for more information on this technique). We linearly interpolated F_{CO2} + dF between CARVE measurement periods to produce the optimized CO_2 flux for Alaska in 2012-2014. Outside of the

CARVE measurement periods, the additive flux correction was set to zero so the F_{CO2} was adopted, a choice evaluated quantitatively in SM4 below. We calculated the mean and 95% confidence intervals of the 10,000 realizations of the optimized flux to generate the errors in Table 1. Using this method, we also calculated the optimized CO_2 budget for the year for the entire domain and each of the regions shown in Fig. 2.

3.4. Numerical Tests of the Optimization Framework

For each flight period we generated "pseudo-truth" emissions and "pseudo-data" observations, using our complete model-data framework. We then applied the inversion analysis to retrieve an estimate of the pseudo-truth emissions and evaluated the inversion framework by comparing the retrieved estimate to the pseudo-truth emissions. A successful framework would estimate the CO_2 budget within the 95% confidence interval 95% of the time. We repeated this experiment 100 times to obtain a statistically valid sample (while managing computational expense). Pseudo-truth emissions were randomly generated with realistic variations from PVPRM (according to the prior error). Pseudo-data observations were generated by combining the pseudo-truth emissions with STILT footprints for the CARVE flights, and adding error (according to the model-data mismatch error). We also added temporal variability to the pseudo-truth emissions by using two patterns: case 1) an exponential covariance in time with a 5-day time scale, and case 2) scaling to a diurnal cycle of respiration from PVPRM. In case 1) 93.8% of the budgets were within the 95% confidence intervals. In case 2) 94.6% of the budgets were within the 95% confidence intervals. We conclude that the inversion framework estimates the mean CO_2 budget during the flight periods accurately and with well constrained uncertainty.

3.5. Subregions of Alaska

We identified four generalized regions for our spatial analysis: North Slope Tundra, South & West Tundra, Boreal Forests, and Mixed. North Slope Tundra included grid boxes with 60% or more tundra north of 67°N. South & West Tundra included grid boxes with 60% or more tundra south of 67°N. Forests represented areas of at least 40% forest cover within the state. "Mixed" represents everything else not classified in the other regions. NS Tundra, SW Tundra and Forests represent ~80% of the total area of the state.

3.6. Growing Season Length

We determined the length of the growing season overall for Alaska and distinct regions within Alaska, based on the dates that the net CO_2 flux changes from source to sink and sink to source (Fig. 1). The aircraft optimized CO_2 flux shows that net CO_2 uptake began in mid-June and continued until early-mid September, depending on the year, with mean uptake over 87, 84, and 102 days in 2012, 2013 and 2014 respectively. Spring carbon uptake displayed a strong latitudinal gradient in Alaska. In spring, on average over Alaska, net CO_2 uptake began on May 31, June 5 and May 18. However, in 2014 a cold period in late May reduced carbon uptake before resuming again in early June. Net CO_2 uptake in boreal forests regions began 2-5 days before the mean for Alaska. The CO_2 uptake

in both the North Slope and South-West tundra ecosystems began 4-11 days after the mean for Alaska. In late August and early September, net CO_2 emission in the South-West Tundra occurred 5-10 days after the North Slope Tundra, consistent with a latitudinal gradient in environmental drivers, with warmer temperatures in the south allowing for a longer growing season. The net daytime uptake of CO_2 at BRW suggests a much shorter growing season (~51 days, 15 June - 4 August on average for 2002-2016).

4. Validation of regional CO_2 fluxes using tower data

We used the PVPRM fluxes for time periods with no CARVE flights and we evaluated our optimized fluxes for the full year-round by comparison with observations from two long-term towers operating in Alaska. We convolved the optimized fluxes (**SM3**) with the surface influence (WRF-STILT, **SM2.1**) at the towers and evaluated the hourly calculated CO_2 enhancements for well mixed afternoon periods against the observed enhancements. None of these tower data were used in the optimization process.

4.1. The CRV Tower

The CRV Tower, located in Fox, AK (64.986°N, 147.598°W, ground elevation 611 masl (meters above sea level)) is a 32 m tower operated by the National Oceanic and Atmospheric Administration (NOAA), where CO_2 and CH_4 mole fractions are measured continuously **(*6*)**. The tower is located on a ridge with large surface influence from boreal ecosystems to the south, west and east. There is little or no influence on the tower from the North Slope. Continuous *in situ* measurements of CO_2, CH_4 and CO mole fractions were made using either a Picarro G2401- m or G2401 Cavity Ring-Down Spectrometer (CRDS) analyzer. The full description of the instrumental setup and in depth discussion of the calibration of both analyzers is discussed in Karion et al., 2016 **(*6*)**. Background CO_2 mole fractions were calculated using the method described in Karion et al., 2016 **(*6*)** and shown in Fig S2. Since the CRV tower is located on a small ridge that is not well represented in the WRF terrain height field, the effect of varying the height of the receptor location (the WRF-STILT starting location) above the CRV tower was assessed by calculating the surface influence function (**SM2.1**) for three effective receptor heights: 35 m, 100 m and 300 m above model ground level (agl). The differences in the calculated CO_2 enhancement due to the effective receptor height were minimal in summer but notable variability was introduced in winter, where the results at different heights varied by up to 1.5 ppm on an hourly basis. However, monthly mean values were not affected significantly. Figure S10 shows the CO_2 enhancement calculated from the surface influence and the aircraft optimized (**SM3**) CO_2 flux fields.

The CO_2 enhancements calculated from the optimized fluxes captured the increased early winter (September - December) CO_2 enhancements evident in the CRV tower data in periods when aircraft measurements were made, although the magnitude of the early winter respiration from the boreal region was somewhat underestimated in 2013 and 2014. For periods when no aircraft data is available (January - March; JFM), the observed and calculated enhancements agreed well during the Arctic late winter months, when snow cover decoupled the air and soil temperatures: the mean observed

CO_2 enhancement was 1.70 ± 0.1 ppm and the calculated CO_2 enhancement was 1.83 ± 0.10, giving a mean difference of only 0.13 ppm (~8%; Fig. S10). This result gives us confidence in adopting the PVPRM-SIF/WRF-STILT calculated fluxes for the wintertime fluxes in boreal ecosystems, including the soil temperature dependence of sub-nivean respiration in late winter.

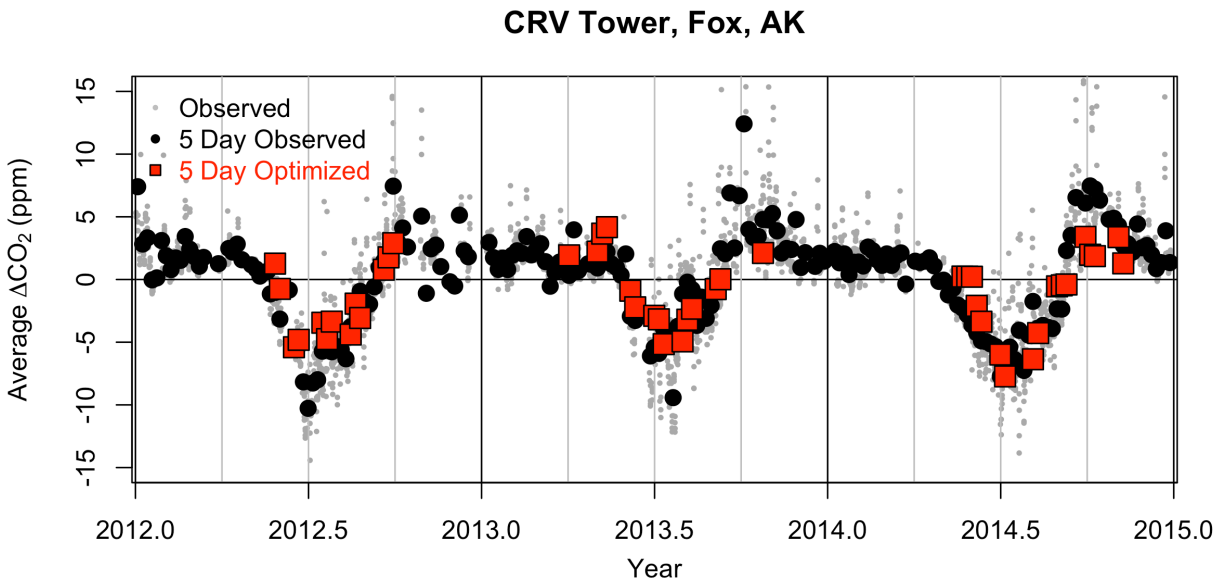

Fig S10: *Mean daytime (11am - 4pm local time (AKST)) CO_2 enhancement (5 day block average) observed at the CRV tower in central Alaska. Observed (grey circles (hourly) and black circles (5 day average)) and optimized CO_2 enhancement (5 day average) at the CRV tower. Only the enhancements calculated during the aircraft optimization period are shown.*

4.2. The BRW Tower

The BRW Tower, located just outside Barrow, AK (71.323°N, 156.611°W, ground elevation 11.00 masl (meters above sea level)), is a 16.46 m tower operated by NOAA since 1973 **(*7*)**, with consistent CO_2 data available from 1975 onwards. The site location was chosen specifically to measure background CO_2 mole fractions; the dominant wind sector samples air from the Arctic Ocean (also known as the "clean air sector"). CO_2 mole fractions at the site are also influenced by CO_2 fluxes from the wider North Slope area from time to time, because of variability in surface winds. The description of the instrumental setup is available in (*7*).

We combined the surface influence from WRF-STILT for the BRW tower (**SM2.1**) with PVPRM-SIF (**SM2.2**) and aircraft optimized (**SM3**) CO_2 flux fields to estimate the atmospheric enhancements in CO_2 expected at the tower. There are insufficient land sector data for a robust analysis of CO_2 fluxes during the growing season, but there are sufficient early and late winter data for testing. We found that, for early winter (September

- December), the CO_2 enhancement calculated from the aircraft optimized CO_2 flux underestimated the observed CO_2 enhancement at the BRW tower data, by about a factor of 2. This model-data difference indicated that the ecosystems near the BRW tower produced somewhat more CO_2 than what was typical for the broader tundra ecosystems types constrained by the CARVE aircraft observations. During the winter months (November - March), when snow cover results in the decoupling of air and soil temperatures, agreement was excellent. The mean observed CO_2 enhancement was 2.21 ± 0.45 ppm and the calculated CO_2 enhancement was 2.22 ± 0.21, giving a mean difference of 0.01 ppm across the winter. This result provided evidence that PVPRM-SIF generated realistic wintertime fluxes in tundra ecosystems, including the soil temperature dependence of respiration in late winter.

5. Long-term BRW CO_2 Observations

After testing the optimization against the BRW tower (**SM4.2**), we analyzed the BRW data to place the CARVE regional fluxes in the context of longer-term changes in North Slope tundra. We selected all valid CO_2 data, regardless of wind direction and retained hourly data with wind speeds above 2.5 m s^{-1}. Results were insensitive to the choice of this threshold between 2.0 and 3.0 m s^{-1}. Strong vertical gradients can develop during periods of light winds that result in the surface influence fields being representative of local areas near the tower rather than of larger areas. We defined background CO_2 mole fractions for this site as air from wind directions of 0° - 45°. This choice of ocean sector is slightly more restrictive than the 0 - 90° used previously ***(36)***. Figure S11 shows our background (0° - 45°, black) selection, which is a subset of the NOAA clean air selection (0° - 90°, blue). Using a wider angle of influence produces similar results but we wanted to clearly exclude influence by the lagoon to the east and the town of Barrow to the west. Slow air-sea gas change minimizes any influence from coastal carbon dynamics and our results are insensitive to the wind direction of the background. We interpolated the background CO_2 mole fractions in time by applying a smooth penalized spline to 10-day average clean air sector data (Fig S11, orange line). The land sector was defined as air arriving at the tower from the south (135° - 202.5°) in order to maximize the influence from the North Slope (Fig 11A-C, red squares). The scaled daily maximum incident solar radiation is also shown in Fig. S11 ***(37)*** .

We used long-term meteorology records to test the adoption of ocean sector CO_2 mole fractions as background for the land sector in our calculation of land sector excess CO_2 (dCO_2), and to test for changes in the magnitude or location of surface influence at the BRW tower. Using the Hybrid Single Particle Lagrangian Integrated Trajectory Model (HYSPLIT, ***(38)***), driven by meteorological fields from NARR (1980 - 2014), we traced back the origin of land sector and ocean sector air using Lagrangian particles generated for each hour of observations at BRW and noted the location where the particles entered the domain (box of approximate latitude 67°N - 73°N and longitude 169°W to 155°W, centered around Barrow, approximately ~10 km off-shore). For the 1980-2014 period, 77% of the land sector air parcels entered the domain to the ocean side, generally in less than 48 hours, as did > 90% of the ocean sector data. Therefore, the ocean sector CO_2

data acts as a background value for the land sector CO_2 data, allowing us to calculate the CO_2 land influence, dCO_2 (ppm). We also found no evidence of any systematic change in the circulation patterns or duration of surface influence from the North Slope over that time.

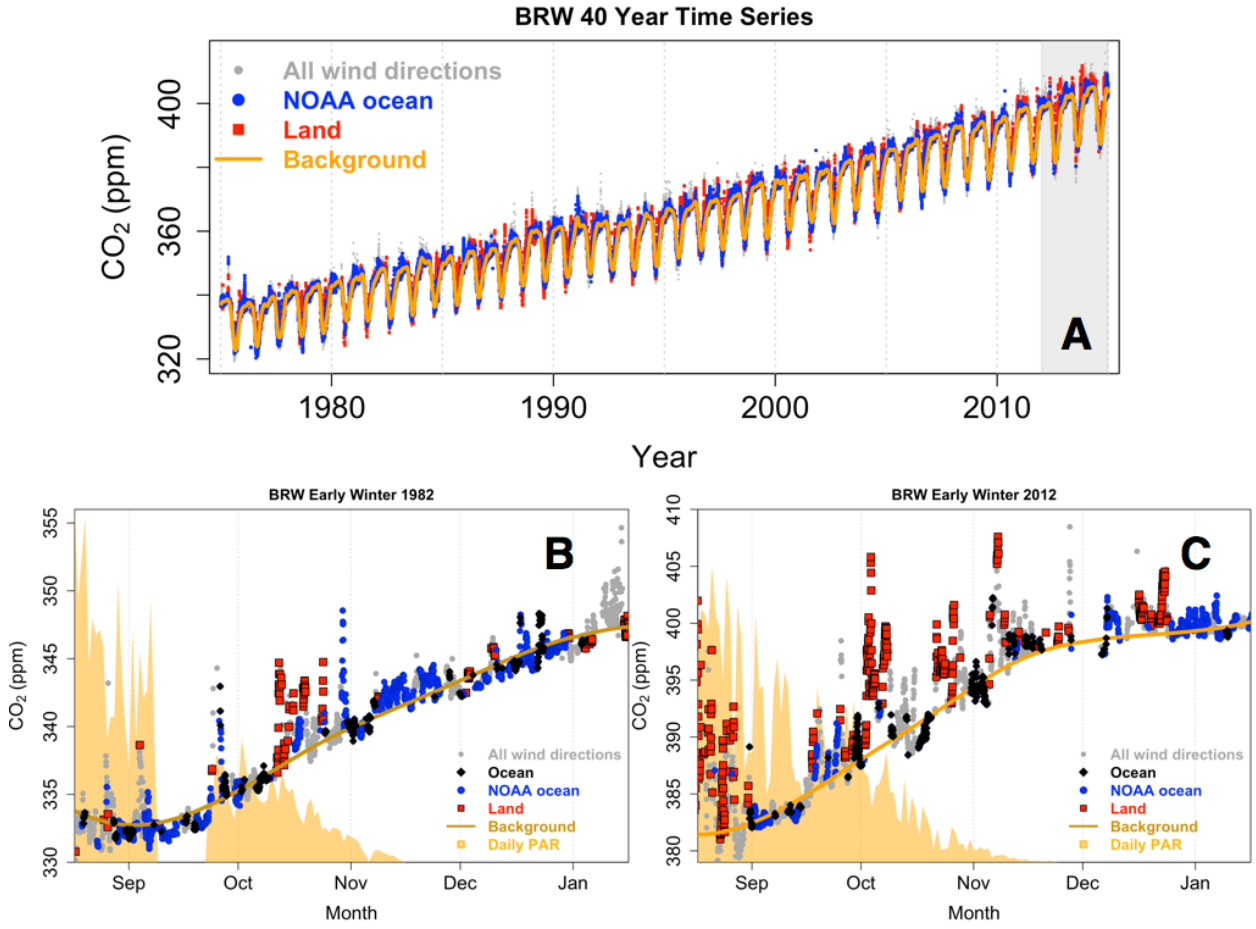

Fig S11: *Time series of BRW CO_2 mole fractions.* ***A*** *CO_2 in air from all wind directions (gray), NOAA ocean sector (blue circles), land sector (red squares) and interpolated BRW background (orange line) for the 40 year time series. Gray shading indicates the time period of the CARVE analysis.* ***B****: Early winter 1982 CO_2 data.* ***C****: Early winter 2012 CO_2 data both show A with the addition of the ocean sector (black) used in our analysis. The peak daytime solar input (scaled to fit the graph) is shown in yellow. Barrow does not see daylight between mid-November and mid-January.*

Sweeney et al (2016) analyzed the long-term methane concentrations at the BRW tower in a similar manner to that employed here for CO_2 (***36***). They used 2m wind speed measured at the tower from the land sector as an indicator of potential changes in boundary layer depth and did not see any change over the course of the record. In con-

trast to our results, they found no significant change in land-sector methane concentration enhancements over the 30-year record of methane observations at the NOAA tower (from 1985 through 2015). With no observed change in methane emission, this would suggest no increase in gas field drilling within the land sector area. Therefore, we believe the calculation of the CO_2 flux described below is representative of the sampled area and sampled time period.

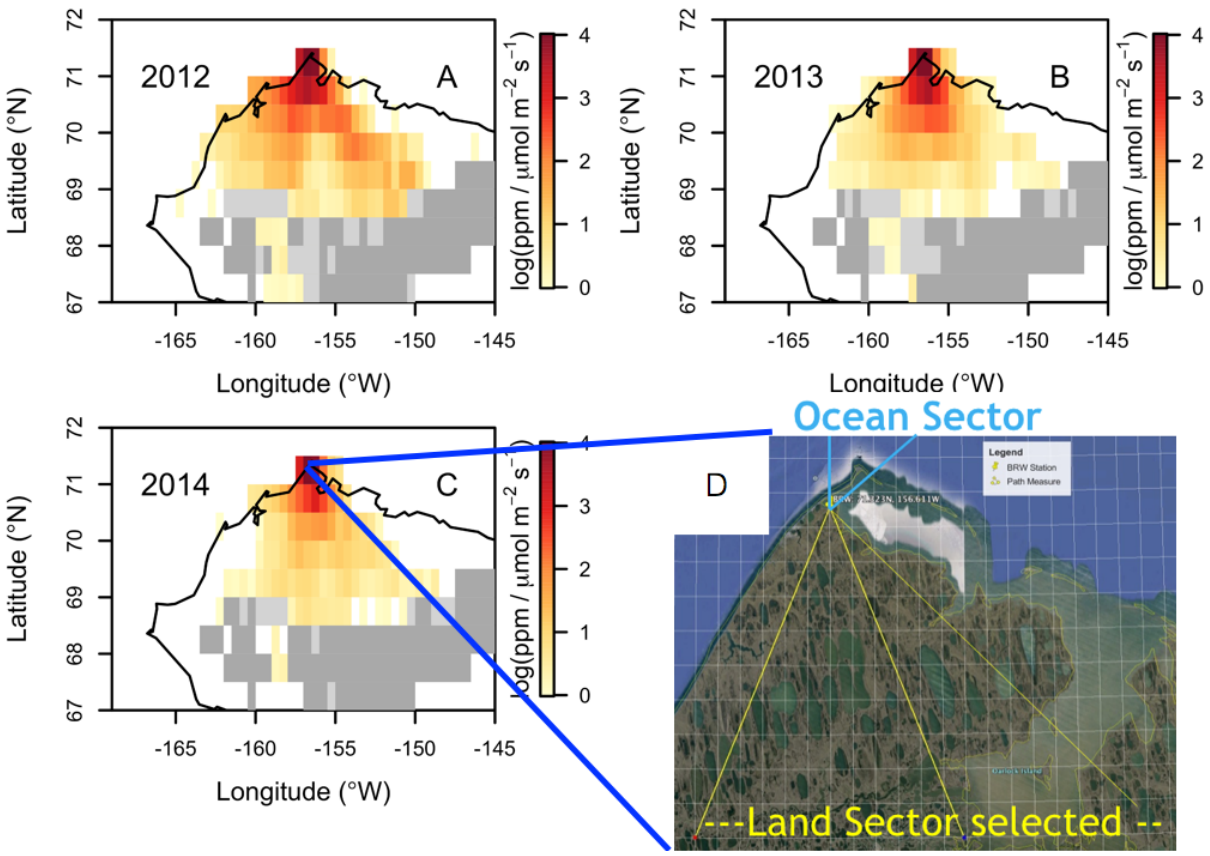

Fig S12: A-C *Summed 5 day land surface influence on BRW tower observations for early winter 2012-2014, when wind directions were from the land sector (135°-202.5°). The spatial extent of the high altitudes of the Brooks Range is shown in gray, with the areas of footprint sampling the mountains shown in light gray.* ***D*** *The location of the tower with extent of land-sector shown between yellow lines. The land sector is defined as 135°-202.5° and the ocean is defined as 0°-45° with respect to the tower.*

We found a significant (73.4% ± 10.8%, 95% C.I.) increase in early winter (October - December) dCO_2 in recent years from 1.5 ± 0.64 ppm in 1975-1989 to 2.62 ± 0.85 ppm in 2004-2015. We calculated the monthly mean dCO_2 for early winter months (September - December) in each 11 year time interval (Fig S13), and, using the years with

data in each month, calculated the 95% confidence interval for the change in dCO_2 over the October-December between 1975-1989 and 2004-2015 (Fig 3). The magnitude of the calculated increase depends on the months used in the analysis. For example, we obtained a 44% ± 6% increase using September - December, a 95% ± 16% increase using data from November and December or 166% ± 4% for December alone. As there is often sparse land sector data in any given year (especially in June and July of most years), we calculated 11 year means across October to December to ensure statistical rigor. Results for changes over the period (1975-2015) were indistinguishable using alternative statistical approaches, including (i) dividing the time period into 2 or 4 subintervals, (ii) linear regressions versus time by month and/or season, or (iii) application of locally-weighted least squares ("loess") to the time series by month or for all fall observations.

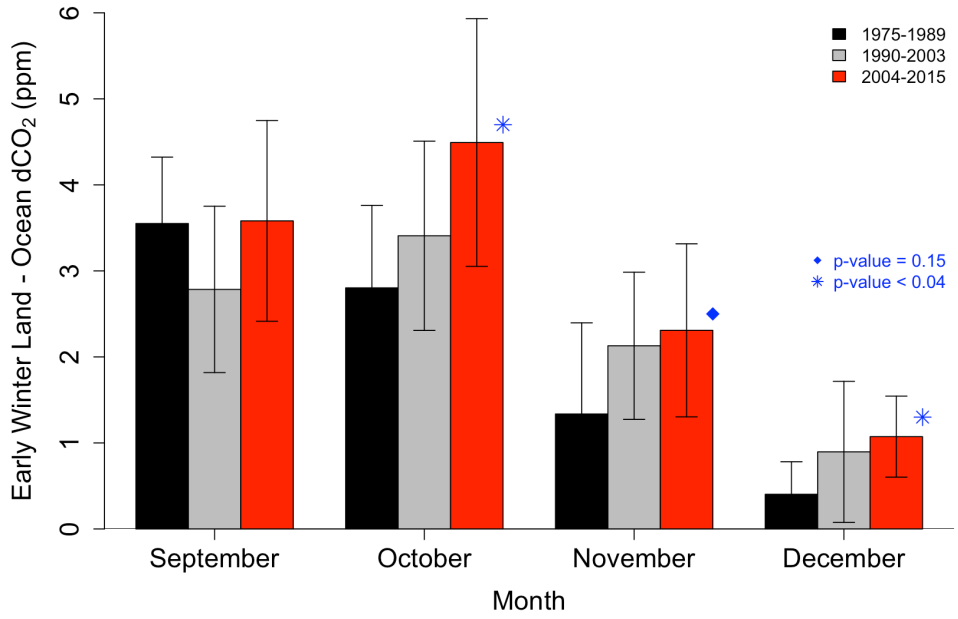

Fig S13: *Early winter Land - Ocean dCO_2 for each month across the 11 year periods of 1975-1989 (black), 1990-2003 (grey), 2004-2015 (red). There are statistically significant increases between the first and last 11 year periods for data obtained in October (p-value < 0.04; 1975-1989 vs 2004-2015, blue asterisks), November (p-value = 0.15; 1975-1989 vs 2004-2015, blue diamond) and December (p-value < 0.04; 1975-1989 vs 2004-2015, blue asterisks).*

Using the land surface influence at the BRW tower (Fig S12A-C), we estimated the flux of CO_2 associated with the early winter CO_2 in 2012-2014. The ratio of the modeled and observed dCO_2 compared to the calculated CO_2 flux allows us to estimate the "observed" CO_2 flux:

$$F^{\mathrm{obs}} = \mathrm{dCO_2^{obs}} \cdot \frac{F^{\mathrm{mod}}}{\mathrm{dCO_2^{mod}}} \tag{8}$$

The model mean F^{mod}/dCO_2^{mod} ratio for October - December was 0.21 µmol m^{-2} s^{-1} ppm^{-1} in 2012-2014 and the mean observed dCO_2 at BRW was 2.93 ppm. Therefore the mean early winter flux estimate for 2012 - 2014 is 0.62 µmol m^{-2} s^{-1}. Assuming the general flux/mole fraction ratio observed at BRW in 2012-2014 is similar to that observed at BRW throughout the 41 year measurement period, the mean flux of CO_2 on the North Slope has increased by 78% from 0.24 µmol m^{-2} s^{-1} in 1975-1989 to 0.43 µmol m^{-2} s^{-1} in 2004-2015. We note that the 2012-2014 flux was nearly 43% higher than the 2004-2015 average. However, there is insufficient data to say if there has been a notably stronger increase in CO_2 emissions in early winter in 2012-2014.

Across the decades, the data suggest possibly accelerated net uptake of daytime CO_2 in the land sector between 1975 and 2005, but in the past 10 years, this daytime net uptake of CO_2 seemed to have been reduced. Our simple analysis does not allow us to robustly separate the photosynthetic and respiration signal during the growing season, due to the covariance of boundary layer height and solar irradiance, so we cannot determine if there is a trend in net uptake fluxes.

SM6. Total Alaskan CO_2 Flux

We calculated the total annual Alaskan flux of CO_2 (Fig. 2c), which includes contributions from the biogenic flux (described in detail above), fossil fuel emissions, and biomass burning emissions.

SM6.1. Fossil Fuel

We did not sample in populated areas, and we excluded data with elevated carbon monoxide (CO) concentrations, so our posterior fluxes do not account for fossil fuel emissions or biomass fires. Fossil fuel emissions from Alaska for 2012-2013 were calculated using values from the Energy Information Administration (EIA, ***(39)***). Emissions for 2014 were extrapolated by scaling the 2013 emissions by the increase of 0.9% in US nation emissions obtained from the BP Statistical Review of World Energy, 2015 ***(40)***. Note that this extrapolation assumes the proportion of Alaska to total USA emissions remains constant between 2013 and 2014. By comparing the emissions for the year 2002 between EIA and the Vulcan Project ***(41)*** we estimate the uncertainty as 10%. Therefore we calculate a total Alaskan fossil fuel emission of 10.3 TgC for 2012, 9.8 TgC for 2013 and 9.9 TgC for 2014.

SM6.2. Biomass Burning emissions of CO_2

Biomass burning emissions of CO_2 were likewise excluded from our biogenic analysis by the CO-filter. We obtained estimates from the Alaskan Fire Emissions Database (AKFED, (***42***)). AKFED is an empirical and remote sensing driven model of daily burned area and carbon consumption by fires at 500 m for Alaska. The updated version of AKFED used here ingests meteorological information from NARR to infer fire weather conditions at the day of burning in addition to remotely sensed pre-fire tree cover and burn severity. AKFED includes uncertainty estimates that accounts for unexplained model variance, uncertainties in the land cover classification and spatial scaling. 2012 (1.59 ± 0.33 Tg C) and 2014 (1.01 ± 0.32 TgC) were relatively low fire years, whereas 2013 had higher pyrogenic CO_2 emissions (13.59 ± 2.84 TgC). Comparison of CO simulated by AKFED emissions coupled to WRF-STILT agreed reasonably well with observations from the CRV tower, providing some confidence that AKFED was able to accurately simulate daily variability in fire emissions and the response of these emissions to changes in meteorology (***43***).

	2012 (TgC), (2.5 and 97.5%CI)	**2013 (TgC)**	**2014 (TgC)**	**Net 2012-2014 (TgC)**
Biomass Burning	1.6 ± 0.3	13.6 ± 2.8	1.0 ± 0.3	16.2
Fossil Fuels	10.3 ± 1.0	9.8 ± 1.0	9.9 ± 1.0	30.0
Total Biogenic	**-5.4 (-23.1, +13.0)**	**44.4 (20.7, 67.4)**	**21.2 (1.2, 41.2)**	**60.4 (24.9, 94.9)**
North Slope Tundra	6.1 (0.5, 22.4)	14.9 (7.5, 22.4)	13.9 (8.5, 19.3)	34.9 (24.1, 45.8)
South-west Tundra	7.1 (3.6, 10.6)	15.7 (8.9, 22.5)	10.5 (5.6, 15.5)	33.3 (24.3, 42.3)
Boreal Forests	-26.7 (-28.6, -15.1)	-3.0 (-14.6,8.7)	-18.2 (-30.6,-5.4)	-48.1 (-68.5, -27.0)
Mixed areas	8.1	16.8	15.0	40.3

Table S1: CO_2 flux from Alaska (TgC yr^{-1}). Annual Biomass Burning, Fossil Fuel and Total Biogenic Carbon budget for Alaska (TgC). Biogenic flux from the regional ecosystems in Alaska: North Slope Tundra, South-west Tundra, Boreal Forests, Mixed area ecoregions.

SM7. Coupled Model Intercomparison Project 5 (CMIP5)

We examined the Alaskan CO_2 fluxes from the earth system model (ESM) simulations contributed to the Coupled Model Intercomparison Project Phase 5 (CMIP5) (***44***). We analyzed future ESM projections forced with Representative Concentration Pathway (RCP) 8.5 greenhouse gas concentrations. These simulations, referred to as experiment 4.2 or “rcp85” by Taylor et al. (***44***), span the period of 2006 to 2100 and use atmospher-

ic CO_2 concentrations that are consistent with a rapid economic growth scenario (***45***). We obtained these data from the Earth System Grid Federation (***46***), and extracted monthly mean net ecosystem exchange (NEE) time series from 2006 through 2014, when fossil fuel emissions and CO_2 mole fractions closely matched observations (***47***). The model simulations analyzed here branched in 2006 from a transient historical simulation that spanned 1850-2005 and used observed fossil fuel emissions and other greenhouse and aerosol forcing agents as boundary conditions. We extracted the land fluxes and calculated the area-weighted sum for the Alaska study domain of 58° - 72°N, 140° - 170°W. The ambient air temperature used to drive the CMIP5 simulations closely matched the air temperature over Alaska reported by the Climate Research Unit (CRU) version 3.23 time series (***48***) (Fig S14).

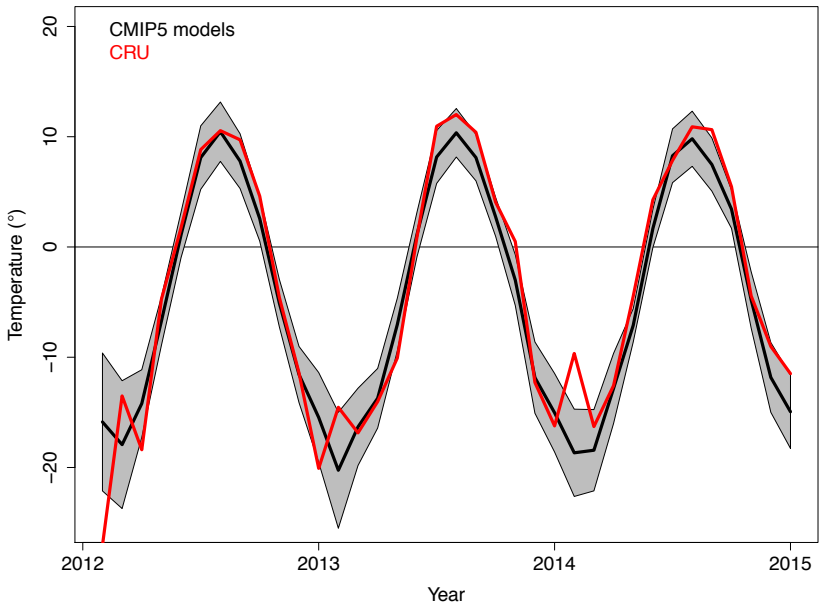

Fig S14: *Time Series of the ambient temperature used in the CMIP5 model simulations. The mean of the models (black solid line) and 95% confidence intervals (grey shading) and the mean ambient temperature of the Climate Research Unit (CRU) over the state of Alaska (red line).*

Using a smoothed spline fit to the monthly data, we calculated the integral of the carbon uptake in summer, the Growing Season Net Flux (GSNF) **(*49*)**, and tabulated the zero crossing dates of net ecosystem exchange in spring and fall, to calculate the net growing season days. CMIP5 model estimates of high latitude carbon exchange spanned a very wide range (Table S1). Note: INMCM4 reported substantial uptake throughout the year, which is clearly erroneous, and this model was removed from further analysis. Some models vastly overestimate (bcc-csm1-1, HadGEM2-ES, IPSL-CM5A-LR and GFDL-ESM2G) or underestimate (CanESM2, CESM1-BGC and NorESM1-M) the growing sea-

son net flux (Fig 4, Table S1). Three of the CMIP5 models capture the growing season net flux relatively well (MIROC-ESM, MIROC-ESM-CHEM, MPI-ESM-LR), but still underestimate the annual net CO_2 flux, with two of these models calculating a regional net carbon sink, contrary to our observations.

The third model (MIROC-ESM-CHEM) predicts an annual net source of CO_2 but incorrectly predicts peak carbon uptake in June, almost a month earlier than observed (Fig. 4C). The mean growing season length for 2012-2014 using the aircraft-optimized estimate is 92 days. In contrast, the selected CMIP5 models predict a mean of 106 days, a 17% overestimation in the length of the growing season (Table S1). The models with the closest summer and winter fluxes calculated spring-time net uptake too early by between 12 and 23 days (MPI-ESM-LR (12 days), MIROC-ESM (21 days), MIROC-ESM-CHEM (23 days), Table S1).

Model	Annual Budget (TgC)	GSNF (TgC)	Relative Spring Zero Crossing
Optimized PVPRM-SIF (oNEE)	**42.9**	**-201.8**	
PVPRM-SIF	-37.0	-214.5	3
PVPRM-EVI	-102.7	-257.4	19
MIROC-ESM	-1.9	-175.3	23
MIROC-ESM-CHEM	24.7	-159.0	25
MPI-ESM-LR	-69.3	-152.8	15
HadGEM2-ES	-138.8	-398.5	3
IPSL-CM5A-LR	-45.8	-391.9	-3
bcc-csm1-1	-102.0	-302.3	24
CanESM2	22.2	-82.2	-14
CESM1-BGC	-2.7	-52.8	44
NorESM1-M	0.64	-36.2	41
GFDL-ESM2G	-323.4	-568.7	39

Table S2: *A comparison of the CMIP5 models with our base model and the aircraft optimized PVPRM-SIF. The mean annual budget for 2012-2014, the mean Growing Season Net Flux (GSNF) for 2012-2014 and the mean spring zero crossing date relative to the aircraft optimized CO_2 flux for 2012-2014. Positive indicates spring net uptake occurring before the aircraft optimized fluxes, negative indicates later net uptake. Models within a factor of 2 of the optimized GSNF are highlights in blue. Models outside that criterion are highlighted in yellow. PVPRM-SIF spring net uptake coincides with the aircraft optimize NEE.*

References.

1. A. Karion *et al.*, Long-term greenhouse gas measurements from aircraft. *Atmospheric Measurement Techniques*. **6**, 511–526 (2013).
2. R. Y. W. Chang *et al.*, Methane emissions from Alaska in 2012 from CARVE airborne observations. *Proceedings of the National Academy of Sciences of the United States of America*. **111**, 16694–16699 (2014).
3. W. W. Chou, Net fluxes of CO_2 in Amazonia derived from aircraft observations. *Journal of Geophysical Research*. **107** (2002), doi:10.1029/2001jd001295.
4. S. Wofsy, W. Kaplan, R. Harriss, Carbon dioxide in the atmosphere over the Amazon basin. *Journal of Geophysical Research*. **93**, 1377 (1988).
5. L. V. Gatti *et al.*, Drought sensitivity of Amazonian carbon balance revealed by atmospheric measurements. *Nature*. **506**, 76–80 (2014).
6. A. Karion *et al.*, Investigating Alaskan methane and carbon dioxide fluxes using measurements from the CARVE tower. *Atmospheric Chemistry and Physics*. **16**, 5383–5398 (2016).
7. K. Thoning, D. R. Kitzis, A. Crotwell, Atmospheric Carbon Dioxide Dry Air Mole Fractions from quasi-continuous measurements at Barrow, Alaska. *gis.ncdc.noaa.gov*. **2014-08,** doi:10.7289/V5RR1W6B.
8. J. M. Henderson *et al.*, Atmospheric transport simulations in support of the Carbon in Arctic Reservoirs Vulnerability Experiment (CARVE). *Atmospheric Chemistry and Physics* **15**, 4093–4116 (2015).
9. K. A. Luus, *et al.,* Tundra photosynthesis captured by satellite-observed solar-induced chlorophyll fluorescence, *Geophysical Research Letters*, doi:10.1002/2016GL070842, (2017).
10. F. Mesinger *et al.*, North American Regional Reanalysis. *Bulletin of the American Meteorological Society*. **87**, 343–360 (2006).
11. J. Joiner *et al.*, The seasonal cycle of satellite chlorophyll fluorescence observations and its relationship to vegetation phenology and ecosystem atmosphere carbon exchange. *Remote Sensing of Environment*. 152, 375–391 (2014).
12. A. Huete, C. Justice, W. Van Leeuwen, MODIS Vegetation Index (MOD13). *Algorithm Theoretical Basis Document*. 3 (1999).
13. D. K. Hall, G. A. Riggs, V. V. Salomonson, N. E. DiGirolamo, K. J. Bayr, MODIS snow-cover products. *Remote Sensing of Environment*. 83, 181–194 (2002).
14. MODIS Land Science Team MODIS Adaptive Processing System MODAPS, MODAPS Services - About (2015), doi:10.5067/MODIS/MOD09.NRT.006.
15. Z. Wang, C. Liu, A. Huete, From AVHRR-NDVI to MODIS-EVI: Advances in vegetation index research. *Acta Ecologica Sinica*. 23, 979–987 (2003).
16. K A. Luus, J. C. Lin, The Polar Vegetation Photosynthesis and Respiration Model: a parsimonious, satellite-data-driven model of high-latitude CO_2 exchange. *Geoscientific Model Development*. 8, 2655–2674 (2015).
17. P. Mahadevan *et al.*, A satellite–based biosphere parameterization for net ecosystem CO_2 exchange: Vegetation Photosynthesis and Respiration Model (VPRM). *Global Biogeochemical Cycles*. 22, GB2005 (2008).

18. C. Frankenberg *et al.*, Prospects for chlorophyll fluorescence remote sensing from the Orbiting Carbon Observatory-2. *Remote Sensing of Environment*. 147, 1–12 (2014).
19. K. A. Luus, J. C. Lin, CARVE Modeled Gross Ecosystem CO_2 Exchange and Respiration, Alaska, 2012-2014. *ORNL DAAC, Oak Ridge, Tennessee, USA.* (2016), doi: 10.3334/ORNLDAAC/1314.
20. D. A. Walker *et al.*, The Circumpolar Arctic vegetation map. *Journal of Vegetation Science*. 16, 267–282 (2005).
21. M. Jung, K. Henkel, M. Herold, G. Churkina, Exploiting synergies of global land cover products for carbon cycle modeling. *Remote Sensing of Environment*. 101, 534–553 (2006).
22. E. Euskirchen, M. S. Bret-Harte, G. R. Shaver, C. W. Edgar, V. E. Romanovsky, Long-term release of carbon dioxide from arctic tundra ecosystems in Alaska. *Ecosystems*, 1–37 (2016).
23. W. C. Oechel *et al.*, Acclimation of ecosystem CO_2 exchange in the Alaskan Arctic in response to decadal climate warming. *Nature*. **406**, 978–981 (2000).
24. W. C. Oechel, C. A. Laskowski, G. Burba, B. Gioli, A. A. M. Kalhori, Annual patterns and budget of CO_2 flux in an Arctic tussock tundra ecosystem. J. Geophys. Res. Biogeosci. 119, 323–339 (2014).
25. M. Ueyama, H. Iwata, Y. Harazono, Autumn warming reduces the CO_2 sink of a black spruce forest in interior Alaska based on a nine−year eddy covariance measurement. *Global Change Biology*. **20**, 1161–1173 (2014).
26. A. L. Dunn, C. C. Barford, S. C. Wofsy, M. L. Goulden, B. C. Daube, A long-term record of carbon exchange in a boreal black spruce forest: means, responses to interannual variability, and decadal trends. *Global Change Biology*. **13**, 577–590 (2007).
27. A. M. Michalak, L. Bruhwiler, P. P. Tans, A geostatistical approach to surface flux estimation of atmospheric trace gases. *Journal of Geophysical Research: Atmospheres*. 109 (2004), doi:10.1029/2003JD004422.
28. N. Y. Krakauer, T. Schneider, J. T. Randerson, S. C. Olsen, Using generalized cross−validation to select parameters in inversions for regional carbon fluxes. *Geophysical Research Letters*. 31, L19108 (2004).
29. D. Zona *et al.,* Cold season emissions dominate the Arctic tundra methane budget. *Proceedings of the National Academy of Sciences of the United States of America*. **113**, 1, 40-45, doi:10.173/pnas.1516017113 (2016).
30. T. Lauvaux *et al.*, Network design for mesoscale inversions of CO_2 sources and sinks. *Tellus B*. 64, 71 (2012).
31. T. Lauvaux, K. J. Davis, Planetary boundary layer errors in mesoscale inversions of column-integrated CO 2 measurements. *Journal of Geophysical Research: Atmospheres*. 119, 490–508 (2014).
32. K. L. Mueller, V. Yadav, P. S. Curtis, C. Vogel, A. M. Michalak, Attributing the variability of eddy−covariance CO2 flux measurements across temporal scales using geostatistical regression for a mixed northern hardwood, *Global Biogeochemical Cycles*. 24, doi:10.1029/2009GB003642 (2010)

33. S. M. Gourdji *et al.*, North American CO_2 exchange: inter- comparison of modeled estimates with results from a fine-scale atmospheric inversion. *Biogeosciences*. 9, 457–475 (2012).
34. Y. Fang, A. M. Michalak, Y. P. Shiga, V. Yadav, Using atmospheric observations to evaluate the spatiotemporal variability of CO_2 fluxes simulated by terrestrial biospheric models. *Biogeosciences*. 11, 6985–6997 (2014).
35. Y. P. Shiga, A. M. Michalak, S. M. Gourdji, K. L. Mueller, V. Yadav, Detecting fossil fuel emissions patterns from subcontinental regions using North American in situ CO_2 measurements. *Geophysical Research Letters*. 41, 4381–4388 (2014).
36. C. Sweeney *et al.*, No significant increase in long-term CH_4 emissions on North Slope of Alaska despite significant increase in air temperature. *Geophysical Research Letters* (2016), doi:10.1002/2016gl069292.
37. R. Stone *et al.*, BRW Rad & Met Measurements 1992 - 1994. *NOAA Data Report ERL CMDL-*, 1–87 (1996).
38. A. F. Stein, R. R. Draxler, G. D. Rolph, NOAA's HYSPLIT atmospheric transport and dispersion modeling system. *Bulletin of the American Meteorological Society*. 96, 2059– 2077 (2015).
39. U. S. EIA, U.S. Energy Information Administration (EIA) State Carbon Dioxide Emissions, (available at http://www.eia.gov/environment/emissions/state/).
40. BP, BP Statistical Review of World Energy (2016), (available at http://www.bp.com/content/dam/bp/pdf/energy-economics/statistical-review- 2016/bp-statistical-review-of-world-energy-2016-full-report.pdf).
41. K. R. Gurney *et al.*, High Resolution Fossil Fuel Combustion CO_2 Emission Fluxes for the United States. *Environmental Science & Technology*. 43, 5535–5541 (2009).
42. S. Veraverbeke, B. M. Rogers, J. T. Randerson, Daily burned area and carbon emissions from boreal fires in Alaska. *Biogeosciences*. **12**, 3579–3601 (2015).
43. E. Wiggins, et al., The influence of daily meteorology on boreal fire emissions and regional trace gas variability, JGR-Biogeosciences, 121, 2793-2810, doi: 10.1002/2016JG003434 (2016).
44. K. E. Taylor, R. J. Stouffer, G. A. Meehl, An Overview of CMIP5 and the Experiment Design. *Bulletin of the American Meteorological Society*. **93**, 485–498 (2012).
45. Moss, R. H., et al., The next generation of scenarios for climate change research and assessment, Nature, 463(7282), 747–756, doi:10.1038/nature08823 (2010).
46. Williams, D. N., et al., The Earth System Grid Federation: Software framework supporting CMIP5 data analysis and dissemination, CLIVAR Exchanges, 16(2), 40–42 (2011).
47. C. L. Quéré *et al.*, Global Carbon Budget 2015. *Earth System Science Data*. **7**, 349–396 (2015).
48. Harris, I. P. D. J., et al. "Updated high-resolution grids of monthly climatic observations–the CRU TS3. 10 Dataset." International Journal of Climatology, 34.3, 623-642 (2014).

49. I. Fung, K. Prentice, E. Matthews, J. Lerner, G. Russell, Three–dimensional tracer model study of atmospheric CO2: Response to seasonal exchanges with the terrestrial biosphere. *Journal of Geophysical Research: Atmospheres*. 88, 1281–1294 (1983).